

Highly Porous Polyhedral Silsesquioxane Polymers. Synthesis and Characterization

Chunxin Zhang,[†] Florence Babonneau,[‡] Christian Bonhomme,[‡] Richard M. Laine,^{*,†} Christopher L. Soles,[†] Hristo A. Hristov,[†] and Albert F. Yee[†]

Contribution from the Departments of Chemistry, Materials Science and Engineering, and the Macromolecular Science and Engineering Center, University of Michigan, Ann Arbor, Michigan 48109, and Chimie de la Matière Condensée, Université Pierre et Marie Curie Tour 54 E5, 4 Place Jussieu, 75252 Paris Cedex 05, France

Received March 16, 1998

Abstract: Polyhedral octahydridosilsesquioxanes, $[\text{HSiO}_{1.5}]_8$ (**1**) and $[(\text{HSiMe}_2\text{O})\text{SiO}_{1.5}]_8$ (**3**) were hydrosilylatively copolymerized with stoichiometric amounts of the octavinylsilsesquioxanes, $[\text{vinylSiO}_{1.5}]_8$ (**2**) and $[(\text{vinylSiMe}_2\text{O})\text{SiO}_{1.5}]_8$ (**4**) in toluene using platinum divinyltetramethyldisiloxane, "Pt(dvs)", as catalyst. The degree of condensation of the resultant four copolymers ranges from 43% to 81% depending on intercubane chain lengths, as determined by solid state ^{13}C and ^{29}Si MAS NMR analyses, using cross-polarization (CP) techniques. The presence of residual functional groups was confirmed by diffuse reflectance infrared Fourier transform spectroscopy (DRIFTS). Polymer porosities were measured using nitrogen sorption, positron annihilation lifetime spectroscopy (PALS), and small angle X-ray scattering (SAXS) methods. The combination of these three techniques allows a relatively complete description of the pore sizes and pore size distributions in these materials. The pores in the cube interiors are ~ 0.3 nm in diameter, while those between the cubes range from 1 to 50 nm in diameter (for polymer **3** + **4**). Nitrogen sorption analyses give specific surface areas (SSAs) of 380 to 530 m^2/g with "observable" pore volumes of 0.19–0.25 mL/g .

Introduction

Intense efforts have recently been directed toward the development of new micro- and mesoporous materials because of their utility and potential utility as catalysts and catalyst supports,¹ dielectric materials for electronic applications,² media for optical³ and sensor⁴ applications, and selective permeability membranes.⁵ The most extensively explored synthetic approach is via sol-gel polymerization of tri- or tetraalkoxysilanes and other metal alkoxides.⁶ Controlled hydrolysis and condensation of silanes under acidic or basic conditions result in cross-linked gels that can be air-dried to give xerogels or supercritically dried

to produce aerogels. For example, Loy/Shea and Moreau have developed polysilsesquioxane aerogels based on organo-bridged bis(trialkoxo)silanes that provide access to micro- and mesoporous materials with surface areas up to 1000 m^2/g , pore volumes up to 0.6 mL/g , and very well defined micro- and/or mesoporosity.⁷

Unfortunately, sol-gel processing often requires long reaction times (days for some zeolites) and/or unusual conditions (e.g. supercritical drying) to realize the desired properties. Furthermore, sol-gel processing often leads to materials that are hydrophilic due to large numbers of residual hydroxyl groups.⁸ Taken *in toto*, these factors decrease the availability and general utility of sol-gel derived porous materials. Thus, simple and inexpensive alternative routes to controlled porosity materials still represent an important synthetic goal.

Polyhedral silsesquioxanes, particularly the cubic $[(\text{RSiO}_{1.5})_8]$ octamers, offer 4,4' cage structures akin to those found in Linde A and related zeolites.⁹ Zeolites are the epitome of high surface

[†] University of Michigan.

[‡] Université Pierre et Marie Curie Tour 54 E5.

(1) (a) Foley, H. C. In *Perspectives in Molecular Sieve Science*; Flank, W. H., Whyte, T. E., Eds.; ACS Symp. Ser. No. 368; American Chemical Society: Washington, DC, 1988; p 335. (b) Tsurita, Y.; Wada K. *Bull. Chem. Soc. Jpn.* **1997**, *70*, 283. (c) Lopez, T.; Moran, M.; Navarrete, J.; Herrera, L.; Gomez, R. *J. Non-Cryst. Solids* **1992**, *147&148*, 753. (d) Lopez, T.; Bosch, P.; Navarrete, J.; Asomoza, M.; Gomez, R. *J. Sol-Gel Sci. Technol.* **1994**, *1*, 193.

(2) Jeng, S.-P.; Taylor, K.; Seha, T.; Chang, M.-C.; Fattaruso, J.; Havemann, R. H. *VLSI Technology Symposium Digest* **1995**, 61.

(3) (a) Shea, K. J.; Loy, D. A.; Webster, O. *J. Am. Chem. Soc.* **1992**, *114*, 6700. (b) Oviatt, H. W.; Shea, K. J.; Kalluri, S.; Shi, Y.; Steier, W. H. *Chem. Mater.* **1995**, *7*, 493. (c) Rubinsztajn, S.; Zeldin, M.; Fife, W. K. *Macromolecules* **1991**, *24*, 2682. (d) Hsuie, G.-H.; Lee, R.-H.; Jeng, R.-J. *Chem. Mater.* **1997**, *9*, 883. (e) Dunn, B.; Zink, J. I. *J. Mater. Chem.* **1991**, *1*(6), 903.

(4) (a) Bein, T.; Brown, K.; Frye, G. C.; Brinker, C. J. *J. Am. Chem. Soc.* **1989**, *111*, 7640. (b) Aylott, J. W.; Richardson, D. J.; Russell, D. A. *Analyst* **1997**, *122*, 77–80. (c) Lee, S.-K.; Okura, I. *Analyst* **1997**, *122*, 81.

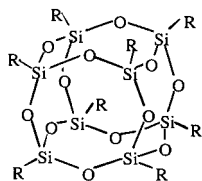
(5) (a) Leenaars, A. F. M.; Keizer, K.; Burggraaf, A. J. In *Reverse Osmosis and Ultrafiltration*; Sourirajan, S., Matsuura, T., Eds. ACS Symp. Ser. No. 281; American Chemical Society: Washington, DC, 1985; p 57. (b) Dire, S.; Pagani, E.; Babonneau, F.; Ceccato, R.; Carturan, G. *J. Mater. Chem.* **1997**, *7*(1), 67. (c) Okui, T.; Saito, Y.; Okubo, T.; Sadakata, M. *J. Sol-Gel Sci. Technol.* **1995**, *5*, 127.

(6) (a) Brinker, C. J.; Scherer, G. W. *Sol-Gel Science: The Physics and Chemistry of Sol-Gel Processing*; Academic Press, Boston, 1990. (b) *Sol-Gel Science and Technology*; Pope, E. J. A., Sakka, S., Klein, L. C., Eds.; American Ceramic Society: Ohio, 1997.

(7) (a) Loy, D. A.; Shea, K. J. *Chem. Rev.* **1995**, *95*, 1431. (b) Shea, K. J.; Loy, D. A. *Chem. Mater.* **1989**, *1*(6), 572. (c) Shea, K. J.; Loy, D. A.; Small, J. H. *Chem. Mater.* **1992**, *4*(2), 255. (d) Loy, D. A.; Russick, E. M.; Yamanaka, S. A.; Baugher, B. M. *Chem. Mater.* **1997**, *9*, 2264. (e) Oviatt, H. W.; Shea, K. J.; Small, J. H. *Chem. Mater.* **1993**, *5*(7), 943. (f) Corriu, R. J. P.; Moreau, J. J. E.; Thepot, P.; Man, M. W. C. *Chem. Mater.* **1996**, *8*, 100. (g) Corriu, R. J. P.; Moreau, J. J. E.; Thepot, P.; Man, M. W. C. *Chem. Mater.* **1992**, *4*, 1217.

(8) Mackenzie, J. D. In *Sol-Gel Science and Technology*; Pope, E. J. A., Sakka, S., Klein, L. C., Eds.; American Ceramic Society: Ohio, 1997; pp 25–32.

(9) Breck, D. W. In *Zeolite Molecular Sieves*; Wiley: New York, 1984; Chapter 2.



- 1, R = H, octahydrodoctasilsesquioxane [HSiO_{1.5}]₈, T₈^H
 2, R = vinyl, octavinylsilsesquioxane [vinylSiO_{1.5}]₈, T₈^V
 3, R = OSi(CH₃)₂H, octa(hydridodimethylsiloxy)silsesquioxane [(HSiMe₂O)SiO_{1.5}]₈, Q₈M₈^H
 4, R = OSi(CH₃)₂vinyl, octa(vinyl dimethylsiloxy)silsesquioxane [(vinylSiMe₂O)SiO_{1.5}]₈, Q₈M₈^V

Figure 1. Hydrido and vinyl cubes 1–4.

area, controlled porosity materials and are typically made by hydrothermal processes. In principle, the polymerization of selected organofunctional cubic silsesquioxanes could offer access to organic/inorganic hybrids with controlled surface area, porosity, and functionality via nonaqueous methods. Based on our interest in developing functionalized “cubic” precursors to hybrid composites,¹⁰ we sought to explore their utility in preparing controlled porosity materials. The goal of the work here is to develop a detailed understanding of the factors that control the porosity of hybrid composites produced by hydrosilylation. Once these factors are identified, it may be possible to establish structure–property relationships that permit the synthesis of hybrids with controlled surface area, porosity, and functionality.

Catalytic hydrosilylation is a well-studied method of forming Si–C linkages by adding Si–H moieties to C–C multiple bonds. Hydrosilylation can be effected under mild conditions in nonaqueous environments. Thus in principle, hydrosilylative copolymerization of simple vinyl- and hydrido-functionalized cubes, e.g., compounds 1–4 in Figure 1, should provide access to copolymers with well-defined structures (Figure 2). For clarity, compounds 3 and 4 are defined as “spacer” analogs of 1 and 2, respectively, because a SiMe₂O spacer is introduced between the cubic cores and the functional groups.

The work of Loy/Shea and Moreau coupled with the synthetic approach suggested in Figure 2 illustrates two complementary approaches to organic/inorganic hybrids. In the first case, the inorganic –O–Si–O– moieties are built up through hydrolysis and condensation of bistralkoxysilane monomers with the organic portion retained intact. In Figure 2 the opposite occurs; the organic bonding between the preformed inorganic cubic silsesquioxane cores is formed last through hydrosilylation. The Shea/Loy and Moreau approach has the advantage of adjusting the pore size by changing organic spacers, while the hydrosilylative approach here may provide better control over homogeneity and pore size distribution in the final products.

Other researchers have also shown that organofunctional cubic silsesquioxanes can be polymerized to form porous hybrid polymers.¹¹ Unfortunately, the various studies on these quite similar cubes and their reactions led to conclusions that differ considerably. Hoebbel and co-workers reported the first preparation of polymer **D** (from **3** and **4**) and related materials. They reported a BET specific surface area (SSA) for polymer **D** of 250 m²/g. In later studies, they described the syntheses

of **B** (from **1** and **4**), **D**, and the product obtained by reacting **3** with octa(allyldimethylsiloxy) cube. In this study, only **D** was found to be porous, with surface areas of 190–360 m²/g. Based on these results, it was suggested that the length of the bridges between the cubes was a critical factor in determining porosity. Only materials with six-atom bridges, like polymer **D**, were suggested to be porous, while shorter (four-atom) or longer (seven-atom) bridges led to nonporous materials.

Recently, Harrison and Kannengiesser reported SSAs for polymers **A** and **C** prepared by hydrosilylation, of 570 and 150 m²/g, respectively.¹² At the time of this latter report, we had already prepared polymers **A–D**, and preliminary porosity measurements revealed that all of the polymers exhibited high SSAs, even with bridge lengths of two to four atoms (Figure 2).¹³ Based on the work presented below, we suspect that these discrepancies arise as a consequence of differences in synthesis conditions (such as concentrations of the monomers and catalysts, type of solvent, etc. and the conditions used to dry the materials). We describe here standard syntheses of the above polymers, a detailed analysis of the degree of condensation that occurs during polymerization, and a study of the types of pores generated during the cross-linking process.

Experimental Section

Materials. Solvents and Reagents. Toluene for hydrosilylation was distilled from sodium/benzophenone under N₂. All other solvents and reagents were used as received from standard vendors.

Catalyst. Pt(dvs) 2–3 wt % solution in xylene from PCR Inc. was diluted to 2 mM with distilled toluene and stored under N₂.

Synthesis of Cubes 1–4. The synthesis of 1–4 followed literature procedures.¹⁴ Compound **1** was purified by subliming at 80–82 °C/0.05 Torr (yield 20%), while **2** was recrystallized from CH₂Cl₂/methanol (yield 47%). Compounds **3** and **4** were both recrystallized from CH₂Cl₂/methanol with recovered yields of 89% and 83%, respectively. The structures of 1–4 were confirmed by ¹H, ¹³C, ²⁹Si NMR, FTIR, and mass-spectral analysis.

Techniques. Solution NMR Analyses. All solution NMRs were run in CDCl₃ and recorded on a Bruker AM 360 Hz spectrometer. ¹H NMR spectra were collected using a 4000 Hz spectral width, a relaxation delay of 1 s, a pulse width of 83°, and 16 K data points. ¹³C{¹H} NMR spectra were obtained at 90.6 MHz using a 16 000 Hz spectral width, a relaxation delay of 0.2 s, a pulse width of 60°, and 16 K data points. CHCl₃ was used as internal reference for ¹H-NMR (7.259 ppm) and CDCl₃ for ¹³C-NMR (77.23 ppm). ²⁹Si NMR spectra were recorded with the spectrometer operating at 71.5 MHz using 32 000 Hz spectral width, a pulse angle of 90°, a relaxation delay of 10.0 s, 32 K data points, and TMS as external reference.

Solid State NMR Analyses. All analyses were conducted on a MSL300 Bruker spectrometer (Laboratoire Chimie de la Matière Condensée) operating at 75.46 MHz for ¹³C and 59.62 MHz for ²⁹Si. A 7-mm Bruker MAS probe and zirconia rotor were used. All solid samples were spun at 4 kHz. The matching of the cross-polarization Hartmann-Hahn condition (¹H 90° pulse length: 6 μs) was set on adamantane (¹³C) and on the T₈^V cube compound (²⁹Si). Relaxation delays were 6 s. Typical numbers of transients were 296 for a ¹³C and 64 for a ²⁹Si cross polarization (CP) experiment (with variable contact time t_c) and 600 for a ¹³C and 200 for a ²⁹Si IRCP experiment (with variable inversion time t_i). Typical contact times for IRCP experiments were 1–3 ms for ¹³C and 5 ms for ²⁹Si. Exponential broadening (20–40 Hz) was applied before Fourier transformation. Isotropic chemical

(10) (a) Sellinger, A.; Laine, R. M.; Chu, V.; Viney, C. J. *Polym. Sci.: Part A: Polym. Chem.* **1994**, *32*, 3069. (b) Sellinger, A.; Laine, R. M. *Macromolecules* **1996**, *29*, 2327. (c) Sellinger, A.; Laine, R. M. *Chem. Mater.* **1996**, *8*, 1592. (d) Zhang, C.; Laine, R. M. *J. Organomet. Chem.* **1996**, *521*, 199.

(11) (a) Hoebbel, D.; Pitsch, I.; Heidemann, D. *Eurogel'91* **1992**, 467. (b) Hoebbel, D.; Endres, K.; Reinert, T.; Pitsch, I. *J. Non-Cryst. Solids* **1994**, *176*, 179.

(12) Harrison, P. G.; Kannengiesser, R. *Chem. Commun.* **1996**, 415.

(13) Zhang, C.; Baranwal, R.; Laine, R. M. *Polym. Prepr. Am. Chem. Soc. Div. Polym. Chem.* **1995**, *36*, 342.

(14) (a) Agaskar, P. A. *Inorg. Chem.* **1991**, *30*, 2707. (b) Hasegawa, I.; Sakka, S.; Sugahara, Y.; Kuroda, K.; Kato, C. J. *Chem. Soc., Chem. Commun.* **1989**, 208. (d) Hasegawa, I.; Motojima, S. *J. Organomet. Chem.* **1992**, *441*, 373.

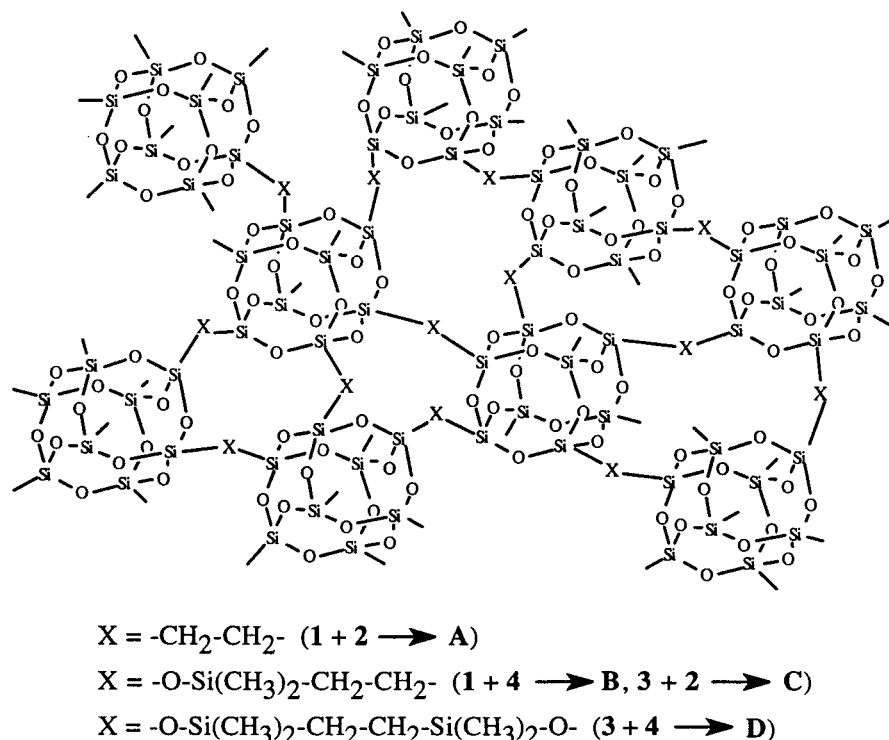


Figure 2. Polymers A–D from cubes 1–4 (β -adducts only). (Polymers B and C are identical.)

shifts are referenced to TMS. Deconvolution of lines were obtained using the WINFIT programs developed by Massiot et al.¹⁵

Mass-Spectral Analyses. Mass-spectra were recorded using a VG analytical model 70-250S mass spectrometer using a DCI probe for both electron impact and ammonia chemical ionization techniques. The electron ionization energy was 70 eV for all analyses. The spectrometer is operated using the 11-250-J data collection software system supplied with the instrument.

DRIFTS. DRIFT spectra were recorded on a Mattson Galaxy Series FTIR 300 spectrometer (Mattson Instruments, Inc., Madison, WI) with a DTGS detector. Random cuttings of crystalline, optical-grade KBr from International Crystal Laboratories, were used to prepare samples. About 600 mg of KBr was ground in a mortar with a pestle, and enough sample was ground with KBr to make a 0.6 wt % mixture. After the sample was loaded, the sample chamber was purged with nitrogen for a minimum of 10 min before data collection. A minimum of 250 scans were collected for each sample at a resolution of $\pm 4 \text{ cm}^{-1}$.

Thermal Analysis. TGA analyses were conducted using a 2950 Thermal Analysis Instruments (TA Instruments, Inc., New Castle, DE) in either flowing air or N_2 . Samples (10–20 mg) were placed in a platinum pyrolysis boat. Mass loss events were followed using a high-resolution (Hi-Res, setting 4) program by which the heating rate is dynamically and continuously modified in response to changes in the decomposition rate of the sample so as to maximize weight change resolution. The maximum ramp rate was $50 \text{ }^\circ\text{C}/\text{min}$. All samples were heated to $950 \text{ }^\circ\text{C}$.

DSC traces were recorded on a 2910 Differential Scanning Calorimeter (TA Instruments, Inc., New Castle, DE) under N_2 . The calorimeter was calibrated using indium as a reference. Samples (5–10 mg) were typically equilibrated at $30 \text{ }^\circ\text{C}$ for 1 min, ramped to the desired temperature at $10 \text{ }^\circ\text{C}/\text{min}$, held at that temperature for 1 min, and allowed to cool back to $30 \text{ }^\circ\text{C}$ naturally. At least three heating-cooling cycles were collected for each analysis.

Specific Surface Area Analyses. Surface areas and pore size distributions were measured by nitrogen sorption at 77 K using the volumetric technique on a Micromeritics ASAP 2000M model instrument (Norcross, GA). Samples were ground and sieved through a 200 mesh sieve and degassed at $80 \text{ }^\circ\text{C}$, $3 \text{ } \mu\text{mHg}$ for $\geq 12 \text{ h}$ before analysis.

SSAs were calculated using the multipoint Brunauer–Emmet–Teller (BET) method using DeltaGraph graphics software. Pore size distributions were determined by density functional theory (DFT) using nitrogen on carbon at 77 K with the slitlike pore model.

PALS Measurements. PALS spectra were collected at various temperatures between -50 and $110 \text{ }^\circ\text{C}$ in air. The positron source was a $35 \text{ } \mu\text{Ci}$ $^{22}\text{NaCl}$ sample deposited between two thin Kapton films. The samples (in powder form) were held between metallic rings ($\approx 3 \text{ mm}$ thick and 6 mm in diameter) covered with Kapton film windows. The positron source was then sandwiched between two such sample holders so that the Kapton windows were directly facing the source. The positron lifetime spectra were obtained by a conventional fast-timing coincidence method. The data were collected with a Micro VAX (Digital model 3100)-based multichannel analyzer. The lifetimes and relative intensities were determined using the conventional FORTRAN program PFPOSFIT. A collection time of 12 h per spectrum was sufficient to reduce the statistical error in τ_3 , I_3 , τ_4 , and I_4 to within $\approx 10\%$.

SAXS. Measurements were performed on a Kratky type camera (Anton Paar, Austria) and Rigaku Giegerflex Cu K_α radiation source operating at 40 kV and 20 mA. The beam was monochromated through a Ni filter and then collimated by an entrance slit of $30 \text{ } \mu\text{m}$ by $\approx 1.2 \text{ cm}$. The diffracted intensities were registered on a position-sensitive proportional counter (M-Braun, Germany Model OED 50) simultaneously for the angles 0.05 – 6.00° in 2θ . The powder samples for the scattering experiments were packed in quartz capillary tubes. The diffraction curves were left in terms of relative scattering intensity but were corrected for air and sample cell scattering as well as sample absorption.

Hydrosilylative Copolymerization of Hydrido and Vinyl Silsesquioxanes 1–4. In current studies, all copolymers were prepared by reacting equimolar amounts of the hydrido and vinyl functionalized cubes in a standard volume of toluene using Pt(dvs) catalyst at 0.01 mol %. Reaction of 1 with 2 provides an example. Octahydridosilsesquioxane 1 (0.600 g, 1.40 mmol) and octavinylsilsesquioxane 2 (0.894 g, 1.40 mmol) were dissolved in 40 mL of dry toluene in a 100 mL of Schlenk flask equipped with a magnetic stirrer. The solution was cooled to $0 \text{ }^\circ\text{C}$, degassed, and purged with N_2 three times under Schlenk line conditions. Then Pt(dvs) solution (2 mM) was added using a 1.0 mL syringe. The reaction was allowed to warm slowly and stirred

(15) Massiot, D.; Thiele, H.; Germanus, A. *Bruker Report* **1994**, 140, 43.

Table 1. Characteristic Parameters for Polymers **A–D**^a

polymer	cubes used	gelation ^b time (h)	R_{hyd} (%)	D ^o cond (%)	SSA ^c (m ² /g, ± std dev)	pore vol ^c (mL/g, ± std dev)
A	1 + 2	9	45	43	529 (± 43)	0.242 (± 0.025)
B	1 + 4	5	71	66	408 (± 23)	0.194 (± 0.010)
C	3 + 2	2	69	68		
D	3 + 4	1	81	82	382 (± 23)	0.203 (± 0.026)

^a Gelation time, extent of hydrosilylation (R_{hyd}) from the ¹³C NMR data, degree of cross-linking (D^o, cond) from the ²⁹Si NMR data and summary of N₂ sorption analysis. ^b Defined as time when magnetic stirring ceases. ^c Results from polymers **B** and **C** do not show significant difference, as they are actually the same structure.

at room temperature. The initially clear solution transforms (quantitatively), after a certain period of time, to a transparent colorless gel, at which point no monomeric silsesquioxanes are detectable (by NMR) in solution. The gelling time, defined as the time where the magnetic stir bar no longer stirs, varies with the cubes used (Table 1). To vary the degrees of condensation of resultant polymers, some of the reactions were further refluxed for 5–10 h but were found to exhibit the same degree of condensation at those not heated (see solid state NMR analyses below). The transparent gel was then collected by suction filtration and dried first in air and then under vacuum at 80 °C (12 h). Significant shrinkage was observed during solvent removal, and brittle, glassy solids were obtained. Samples were ground to fine powders for further characterization.

Results and Discussion

This section is divided into four parts concerned first with copolymer syntheses, followed by microstructural characterization, thermal analyses, and finally porosity studies.

Cube Reactivities. From the gelation times required to prepare polymers **A–D** (Table 1), it can be inferred that the spacer cubes **3** and **4**, are more reactive than nonspacer cubes **1** and **2**, respectively. This could be conveniently explained by steric effects, where the longer and more flexible SiMe₂O spacers give the functional groups on both **3** and **4** more freedom of movement, thus making them more accessible than functional groups on the nonspacer cubes **1** and **2**. However, in earlier hydrosilylation studies with 4-allyloxymethylbenzoate, cube **1**, (HSiO_{1.5})₈, was found to be much more reactive than HMe₂-Si-O-SiMe₂H.^{10a} Because the Si-H environment in HMe₂-Si-O-SiMe₂H resembles that in spacer cube **3**, a closer look at this discrepancy in reactivity becomes necessary.

If only chemical structure is considered here, cube **1** is expected to be more reactive than HMe₂Si-O-SiMe₂H and cube **3** because each Si-H group in cube **1** has two additional electron-withdrawing oxygen atoms which are known to stabilize Si-metal intermediates in hydrosilylation, thereby increasing reactivity.¹⁶ However, if the entire reaction systems are considered, the polymeric system under study here is distinctly different from the 4-allyloxymethylbenzoate system. In reactions of **1** with 4-allyloxymethylbenzoate, even though diffusion of Si-H groups (cubes) in solution is slow because of the high molar mass of the cube, and motion at the cube's surface is restricted by the rigidity of the cube, the vinyl groups of 4-allyloxymethylbenzoate diffuse relatively freely to access Si-H groups on the cube. As a result, the reaction rate is most likely determined by the catalytic cycle.

In contrast, the copolymerization process requires reactive encounters between Si-H and vinyl moieties on two massive cubes. These groups are both sterically and diffusively restricted from reacting, especially after the first coupling

reactions anchor cubes into the growing cross-linked network. For anchored moieties to react they must move toward each other, which means the cubes to which they are attached must also move with them. Because of the bulkiness of the eight armed cubes, they cannot approach each other as freely as small molecules do. Steric hindrance increases coincident with network formation, forcing the remaining functionalities to readjust conformations, further limiting the approach of reactive species. At a certain cross-link density, movement is so sterically restricted as to define equilibrium intercubal distances. These distances define the pores in the polymers. Based on these arguments, the mutual accessibility of two functionalities rather than their chemical reactivities can be expected to dominate the rate and degree of cross-linking in copolymerizations. Since Si-H on the spacer of cube **3** is more accessible, it appears to be more reactive than cube **1**. A similar argument should apply to the reactivity difference between cubes **2** and **4**.

An alternate perspective can be presented if one considers the active catalyst species. If we assume that the first step in the catalytic cycle is oxidative addition of Si-H bonds to metal sites, then completion of the cycle requires that this complex encounter a vinyl group. During polymerization of **1** with **2**, once a single bond between the cubes forms, the catalyst species can either move to adjacent Si-H bonds or diffuse into the reaction solution. Because the local concentration of Si-H bonds is much higher than in solution, the probability is high that the next oxidative addition step will occur locally on the same cube. Then the rate limiting step is defined by the competition between diffusion of unreacted **2** to this new complex or segmental motion that brings a vinyl group on an adjacent, anchored cube close enough for completion of the catalytic cycle.

The same perspective can be used to view the polymerization of **3** and **4**. The differences are that the spacer groups provide better flexibility permitting the reactive moieties to sweep out greater hydrodynamic volumes giving higher effective concentrations microscopically. In addition, the cross-links that contain two spacers enhance segmental motion in anchored cubes thereby adding coupling efficiency. The overall high mobility of reactive functional groups means that the active catalyst species is much less likely to diffuse away from unreacted moieties. The end result appears as a "zipping up" process that suggests self-assembly. Such a zipping up process can be expected to provide better packing of cubes leading to better molecular ordering which coincidentally provides greater control of the pore sizes and size distribution.

In an effort to change the cross-link density of polymers **A–D**, reaction solutions were refluxed for 5–10 h without measurable change in the degree of condensation or the pore size distributions in the final materials (see below). No detailed studies on the effects of variations in other reaction conditions (e.g. solvent type, temperature, catalyst type and concentration, etc.) were conducted; it is likely that these variables will affect the porosity and SSAs of the materials obtained. Some of the discrepancies found in previous reports may arise because different reaction conditions were used.

When **A–D** were subjected to N₂ sorption analyses without first being ground into powder, their SSAs were higher than found with the ground powders. This can be explained by diffusion differences of N₂ in the pores of the powder and blocks of the copolymers. All of the polymers studied here were produced multiple (minimum of three) times with little variation (by MAS-NMR and N₂ sorption analysis).

(16) *Comprehensive Handbook on Hydrosilylation*; Marciniak, B., Ed.; Pergamon Press: 1992.

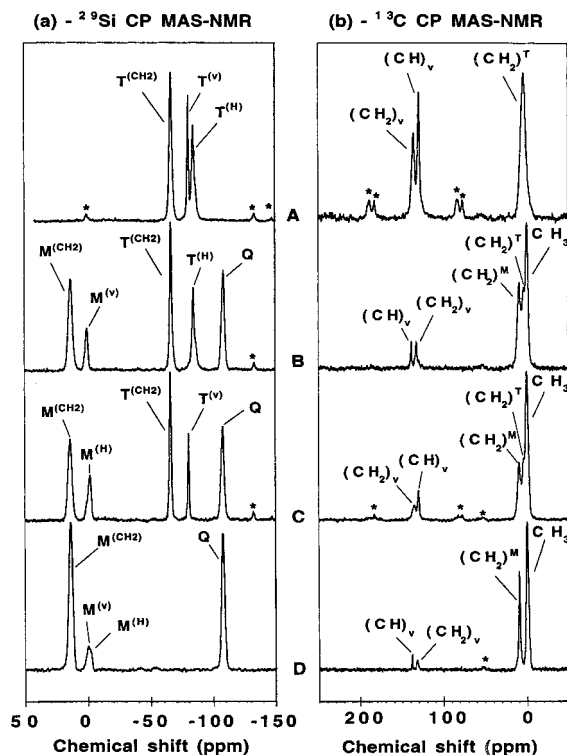


Figure 3. (a) ^{29}Si and (b) ^{13}C MAS-NMR spectra of polymers A–D, recorded with 1 ms (^{13}C) and 5 ms (^{29}Si) contact times. (*: spinning side bands).

Microstructural Characterization. NMR Study of Polymers A–D. The NMR studies were performed to address two main points concerning the structural characterization of the polymers. First, hydrosilylation can produce either linear $\text{Si}-\text{CH}_2-\text{CH}_2-\text{Si}$ (β -hydrosilylation) or branched $\text{Si}-\text{CH}(\text{CH}_3)-\text{Si}$ bridges (α -hydrosilylation). The bridge geometry will certainly affect the development of the network microstructure and therefore the resultant porosity, pore volume, and pore size distribution. Thus, identification of the types and quantification of the bridges that form during hydrosilylation is essential. ^{13}C NMR is an ideal probe to address this point. Analysis of both ^{13}C and ^{29}Si NMR results will give a quantitative estimation of the number of cross-link sites and hence the cross-link density.

Polymers A–D were characterized using both ^{13}C and ^{29}Si solid-state NMR techniques, including cross polarization (CP), magic angle spinning (MAS), and high-power proton decoupling. Examples of ^{13}C and ^{29}Si CP MAS-NMR spectra for these polymers are shown in Figure 3.

^{13}C NMR Peak Assignments. Isotropic chemical shifts (in ppm) as well as line widths (in Hz) for compounds A–D are given as Supporting Information. Residual vinyl sites (CH and CH_2) are characterized by low-field chemical shifts (129.2–138.3 ppm), while aliphatic carbons corresponding to either methyl groups of M units (on spacers of polymers B–D) or the newly formed carbon bridges between cubes appear in the high-field region (–0.8 to –9.3 ppm). The determination of proton multiplicity at a given site (i.e., n for CH_n) can be obtained using a spectral editing sequence, IRCP (inversion recovery cross polarization), which derives from a standard CP sequence based on polarization inversion.^{17,18} In the case of strongly coupled sites, XH_n (i.e., CH and CH_2), analytical expressions of magnetization during the inversion process (t_i) have been derived for powdered samples at moderate MAS ($\ll 10$ kHz), neglecting relaxation¹⁷

$$M_{\text{XH}_n}(t_i) = M^0 \left[\frac{2}{n+1} \exp\left(-\frac{t_i}{T_D}\right) + \frac{2n}{n+1} \exp\left(-\frac{3}{2} \frac{t_i}{T_D}\right) \exp\left(-\frac{t_i^2}{T_C^2}\right) - 1 \right] \quad (1)$$

where t_i is the inversion time, M^0 is the maximum magnetization reached after contact time t_c and “ n ” corresponds to the number of protons directly bonded to X in XH_n (in the present case, $X = ^{13}\text{C}$). The inversion of polarization is characterized by two time constants related to two types of magnetization transfer, T_C and T_D . T_C accounts for coherent magnetization transfer, involving the X nucleus and the directly bonded protons. It is basically a measure of the inverse of the strength of heteronuclear $^1\text{H}-\text{X}$ dipolar coupling in XH_n groups. Rapid molecular motion will lead to a reduction of dipolar coupling which results in an increase of T_C . T_D is related to spin diffusion processes, which involve all the remaining protons. Generally, $T_C \ll T_D$ and the polarization inversion can be described by two regimes: the first regime ($t_i = \text{tens of } \mu\text{s}$ for ^{13}C) is dominated by a rapid decay of the magnetization, characterized by T_C , followed by a much slower inversion regime, characterized by T_D . As the dynamics of the two regimes are very different, a sharp turning point occurs, whose value depends on n of XH_n : for XH ($n = 1$) and XH_2 ($n = 2$), the turning points are 0 and $-1/3$, respectively. In the case of weakly coupled sites (e.g. $\text{C}=\text{O}$, quaternary C), polarization inversion is well described by an exponential process and a unique time constant, T_{XH} , again neglecting relaxation:

$$M(t_i) = M^0 \left[2 \exp\left(-\frac{t_i}{T_{\text{XH}}}\right) - 1 \right] \quad (2)$$

T_{XH} is the standard cross polarization constant. Equation 2 is a standard thermodynamic approach to cross polarization dynamics.¹⁹ CP dynamics can also be studied by variable contact-time experiments as CP and IRCP dynamics are basically the same;²⁰ however, the magnetization of rigid XH_n groups during the contact time varies dramatically for very short contacts (i.e., $t_c \ll 50 \mu\text{s}$). It follows that such experiments will suffer from poor signal/noise ratio (for reasonable acquisition times). Therefore, the IRCP sequence is preferable and provides an invaluable tool for characterizing amorphous derivatives with strongly overlapping peaks.²¹

The ^{13}C IRCP results for polymers A and D are presented in Figure 4. For polymer A, the signal at $\delta = 3.6$ ppm can be simulated with a unique peak, whose corresponding magnetization versus t_i clearly shows two regimes and a turning point at $-1/3$. It can be fit using eq 1 with $n = 2$, $T_C = 21 \pm 1 \mu\text{s}$ and $T_D = 0.7 \pm 0.06$ ms, so the line centered at $\delta = 3.6$ ppm can be safely assigned to methylene CH_2 groups, noted $(\text{CH}_2)^T$. Therefore, the hydrosilylation of 2 with 1 leads primarily to the β -product.

For polymer D, two lines are observed in the aliphatic region at $\delta = -0.4$ and 9.3 ppm. The evolution of magnetization for each line versus t_i is presented in Figure 4. The evolution of the line centered at $\delta = 9.3$ ppm is very similar to that observed for $\delta = 3.6$ ppm in polymer A, for which a turning point at

(17) Wu, X.; Zilm, K. W. *J. Magn. Reson.* **1993**, *A102*, 205.

(18) Wu, X.; Burns, S. T.; Zilm, K. W. *J. Magn. Reson.* **1994**, *A111*, 29.

(19) Pines, A.; Gibby, M. G.; Waugh, J. S. *J. Chem. Phys.* **1973**, *59*, 569.

(20) Wu, X.; Zhang, S.; Wu, X. *Phys. Rev. B* **1988**, *37*, 9827.

(21) Babonneau, F.; Maquet, J.; Bonhomme, C.; Richter, R.; Roewer, G.; Bahloul, D. *Chem. Mater.* **1996**, *8*, 1415.

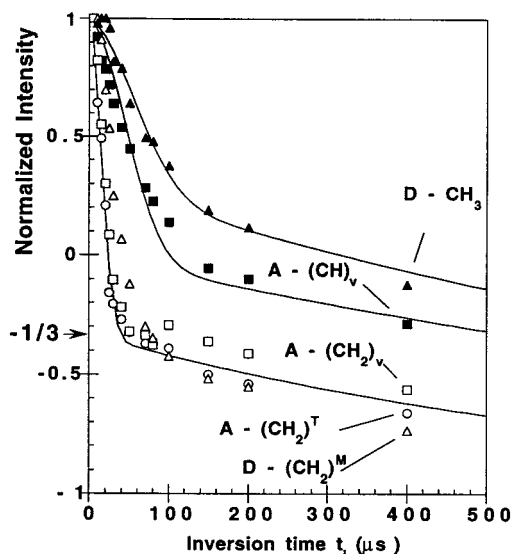


Figure 4. Normalized magnetization evolution versus t_i (inversion time) for ^{13}C sites in polymers **A** and **D**: aliphatic CH_2 in **A** and **D** [$(\text{CH}_2)^{\text{T}}$ and $(\text{CH}_2)^{\text{M}}$], residual vinylic sites in **A** [$(\text{CH})_{\text{v}}$ and $(\text{CH}_2)_{\text{v}}$], and CH_3 in **D**. Chemical shift values are given in Supporting Information. The curves for the residual vinylic sites, given as examples for CH and CH_2 sites, are not discussed in the text.

$\approx -1/3$ is also observed, so it can be assigned to CH_2 . β -Hydrosilylation is thus regarded as the primary polymerization process whereby polymer **D** forms. The extracted T_{C} and T_{D} values are $42 \pm 2 \mu\text{s}$ and $0.5 \pm 0.1 \text{ ms}$, respectively. An increase in T_{C} occurs on going from polymer **A** to **D**. This increase is attributed to a decrease in the dipolar coupling in the methylene groups due to enhanced segmental motion of the flexible spacer of polymer **D**. In support of this, the CH_2 line width in **D** is considerably reduced as compared to the CH_2 line width in **A**.

The line centered at $\delta = -0.4 \text{ ppm}$ is attributed to CH_3 groups in **M** units. Since rapid reorientation of CH_3 groups leads to a substantial reduction in dipolar coupling and an increase in T_{C} ,²² the methyl magnetization is often analyzed with a model involving a unique time constant as in eq 2. However, a nonexponential transfer process involving two time constants for methyl groups has been proposed recently in the literature,²³ and is applied in this study. The evolution versus t_i (see Figure 4) is clearly represented by two regimes, and eq 1 was used to fit the data, with n as a variable parameter. The extracted values are $T_{\text{C}} = 90 \pm 5 \mu\text{s}$, $T_{\text{D}} = 1.5 \pm 0.2 \text{ ms}$, and $n = 0.7$. It follows that a distinction between CH_2 and CH_3 lines is straight forward as the first regime of inversion is much faster for methylene groups. Based on this, the signal at $\approx 0.4 \text{ ppm}$ is assigned to CH_3 in **M** units.

Polymers **B** and **C** are characterized by very similar NMR data as they are virtually of the same chemical structure. The main feature is the presence of two distinct lines in the aliphatic region (3–10 ppm range) whose evolution versus t_i is rapid during the first tens of microseconds, with turning points at $-1/3$. These lines can therefore be assigned to CH_2 groups, corresponding once again to β -hydrosilylation. For polymer **C**, the extracted T_{C} and T_{D} values (eq 1, $n = 2$) are $27 \pm 2 \mu\text{s}$ and $0.75 \pm 0.06 \text{ ms}$, respectively. T_{C} is intermediate between the values obtained for **A** (e.g., $21 \mu\text{s}$) and **D** (e.g., $42 \mu\text{s}$). This

suggests that the amplitude of the local motion increases continuously from **A** to **D**. The assignment of methyl lines is straight forward as they correspond to the most shielded ones ($\approx 0.8 \text{ ppm}$).

In conclusion, the IRCP technique allows us to propose definitive assignments for all ^{13}C lines in polymers **A–D** (see Supporting Information) and shows that β -hydrosilylation is the main cross-linking reaction. Moreover, segmental motion of the bridging carbons was detected along the transition from polymer **A** to **D**, with **D** exhibiting the most motion, which implies that on a segmental scale **D** is more flexible.

Quantitative Measurements Based on ^{13}C NMR. It is generally understood that a CP experiment involving a single contact time is not quantitative. However, when the ^{13}C nuclei are in close contact with the ^1H spin bath, variable contact time experiments are capable of producing quantitative results. Variable contact time experiments were performed on polymers **A–D** to quantify the residual vinylic groups and therefore obtain the extent of hydrosilylative cross-linking for each polymer. The CH_n magnetization can be expressed versus contact time, t_{c} , with the following eq 3:¹⁷

$$M_{^{13}\text{C}_n}(t_{\text{c}}) = M^0 \left[1 - \frac{1}{n+1} \exp\left(-\frac{t_{\text{c}}}{T_{\text{D}}}\right) - \frac{n}{n+1} \times \exp\left(-\frac{3}{2} \frac{t_{\text{c}}}{T_{\text{D}}}\right) \exp\left(-\frac{t_{\text{c}}^2}{T_{\text{C}}^2}\right) \right] \exp\left(-\frac{t_{\text{c}}}{T_{1\rho}^{\text{H}}}\right) \quad (3)$$

T_{C} , T_{D} , and “ n ” have the same meaning as in eq 1, $T_{1\rho}^{\text{H}}$ is the relaxation time of ^1H in the rotating frame. The extracted values for them are given in the Supporting Information. CH and CH_2 magnetization evolution can be fit using eq 3 with $n = 1$ and $n = 2$, respectively, to evaluate the relative amount of the various **C** sites (Table 1). CH_3 magnetization evolution was fit using “ n ” as an extra parameter, just as in the previous qualitative analysis.

Contents of vinyl CH and CH_2 units are similar in all polymers **A–D**, as one would expect. Moreover, the methyl group contents of polymers **B–D** (45%, 48%, and 68%) are in excellent agreement with theory (50%, 50%, and 67%). Such agreement establishes the validity of the quantitative analysis via variable contact time CP experiments.

The extent of the hydrosilylation reaction can be calculated from the amounts of $(\text{CH}_2)^{\text{T}}$ and/or $(\text{CH}_2)^{\text{M}}$ groups and residual vinyl groups according to eq 4:

$$R_{\text{hyd}} = \frac{\%(\text{CH}_2)^{\text{T}} + \%(\text{CH}_2)^{\text{M}}}{\%(\text{CH}_2)_{\text{v}} + \%(\text{CH}_2)_{\text{v}} + \%(\text{CH}_2)^{\text{T}} + \%(\text{CH}_2)^{\text{M}}} \quad (4)$$

The respective extents of reaction are 45%, 71%, 69%, and 81% for polymers **A–D** (Table 1). Obviously, the hydrosilylation process is favored when the vinyl and/or Si–H groups are on **M** rather than **T** units, in another word, if they are on spacer cubes rather than on nonspacer cubes.

^{29}Si Peak Assignments. ^{29}Si NMR spectra for polymers **A–D** are shown in Figure 3a, and isotropic shifts (in ppm) are provided in Supporting Information. No strong overlapping of lines was observed for polymers **A–D**, and assignments were straight forward based on ^{29}Si NMR data for pure cubes **1–4**. However, IRCP can also be used to correlate assignments, and eqs 1 and 2 can be rewritten for SiH_n sites. The magnetization inversion curves for the **Si** sites in polymers **A** and **D** are provided in the Supporting Information.

(22) Alemany, L. B.; Grant, D. M.; Pugmire, R. J.; Alger, T. D.; Zilm, K. W. *J. Am. Chem. Soc.* **1983**, *105*, 2133.

(23) Tekely, P.; Gerardy, V.; Palmas, P.; Canet, D.; Retournard, A. *Solid State Nucl. Magn. Reson.* **1995**, *4*, 361.

For polymer **A**, the three curves corresponding to the peaks at -66.1 ppm ($T^{(\text{CH}_2)}$), -79.9 ppm ($T^{(\text{v})}$), and -84.4 ppm ($T^{(\text{H})}$), can be fit according to eqs 1 and 2 as in the ^{13}C analyses. The first curve corresponding to dynamics of magnetization inversion of the residual $T^{(\text{H})}$ sites is well characterized by two distinct regimes with a turning point of 0. The extracted T_{C} and T_{D} values (using eq 1 and $n = 1$) are 90 ± 10 μs and 2.2 ± 0.5 ms, respectively. It is worth noting that the T_{C} for Si–H is larger than that for rigid CH groups; this can be attributed to a weaker ^{29}Si –H dipolar coupling (lower magnetogyric ratio and longer Si–H bond distance). The other two curves, corresponding to $T^{(\text{CH}_2)}$ and $T^{(\text{v})}$ sites, show an expected monoexponential behavior [eq 2], with $T_{\text{SiH}} = 1.90$ and 2.70 ± 0.05 ms, respectively. The lower value for bridging $T^{(\text{CH}_2)}$ sites can be attributed to a decrease in mobility compared to terminal $T^{(\text{v})}$ sites.

For polymer **D**, the curve related to Q units (-107.8 ppm) can be fit using eq 2, leading to a large T_{SiH} value of 5.2 ± 0.5 ms, which is related to a low ^{29}Si –H dipolar coupling due to long Si \cdots H distances. The other units, $M^{(\text{v})}$ (0.7 ppm), $M^{(\text{CH}_2)}$ (14.0 ppm), and $M^{(\text{H})}$ (-1.6 ppm) do not follow the expected trends. This is due to enhanced segmental motions either in the terminal monofunctional units, $M^{(\text{v})}$ and $M^{(\text{H})}$, or in the bridging units in a flexible spacer, $M^{(\text{CH}_2)}$. This is consistent with the ^{13}C results discussed previously; polymer **D** has greater segmental motion than **A**. The initial rate of magnetization inversion provides an estimation of the ^{29}Si –H dipolar coupling strength with interesting comparisons:

$$T^{(\text{H})} \gg M^{(\text{H})} > M^{(\text{CH}_2)} < M^{(\text{v})}, \quad T^{(\text{CH}_2)} > T^{(\text{v})} > Q$$

The large difference between the $T^{(\text{H})}$ and $M^{(\text{H})}$ units, whose dipolar couplings are both dominated by the interaction with the directly bonded protons, is certainly due to their mobility differences. As part of the polymer network, $T^{(\text{H})}$ units are much more restricted than $M^{(\text{H})}$, which is on the flexible side groups. Interestingly, $M^{(\text{CH}_2)}$ and $M^{(\text{v})}$ units are characterized by higher dipolar coupling values than $T^{(\text{CH}_2)}$ and $T^{(\text{v})}$ units, respectively. In this case, even though $M^{(\text{CH}_2)}$ and $M^{(\text{v})}$ have better mobility than $T^{(\text{CH}_2)}$ and $T^{(\text{v})}$, since the former two units have six protons from bonded methyl groups, they have a greater dipolar coupling than the latter ones, which do not have as many protons.

Quantitative Measurements Based on ^{29}Si NMR. Variable contact time CP experiments were used to quantify different Si sites. The $T^{(\text{H})}$ units can be fit according to a Si version of eq 3 and show the anticipated two-regime behavior characteristic of rigid Si–H entities. The other Si units with a low ^1H – ^{29}Si dipolar coupling can be characterized by a monoexponential build-up of the magnetization versus contact time:

$$M(^{29}\text{Si}) = M^0 \frac{1}{1 - \frac{T_{\text{SiH}}}{T_{1\rho}^{\text{H}}}} \left[1 - \exp\left(-\left(1 - \frac{T_{\text{SiH}}}{T_{1\rho}^{\text{H}}}\right) \frac{t_{\text{c}}}{T_{\text{SiH}}}\right) \right] \exp\left(-\frac{t_{\text{c}}}{T_{1\rho}^{\text{H}}}\right) \quad (5)$$

The extracted parameters from eq 5 allow us to evaluate the relative amounts of the various ^{29}Si sites (see Supporting Information). The reliability of this quantitative analysis can be easily verified: in polymers **B–D**, the amounts of Q units, 29%, 34%, and 51%, respectively, are close to the theoretical values, 33%, 33%, and 50%, respectively. Furthermore, the amounts of $M^{(\text{CH}_2)}$ and $T^{(\text{CH}_2)}$ units in polymers **B** and **C** are quite similar as well as the amounts of residual vinyl and hydrido groups in polymers **C** and **D**. One can argue that this is not the case for

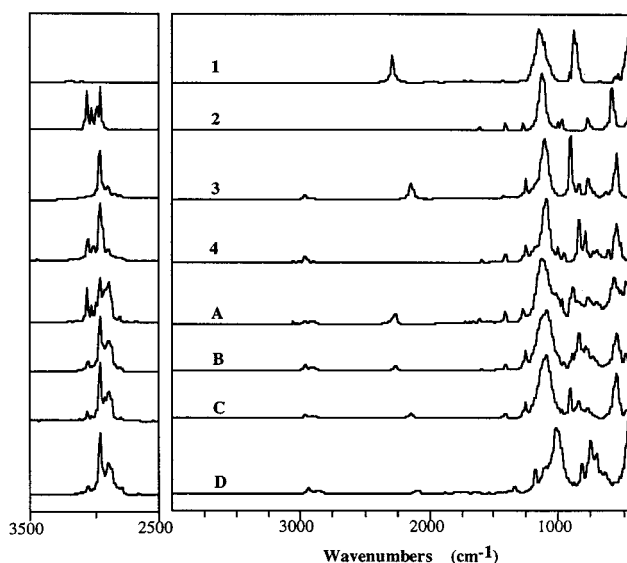


Figure 5. DRIFTS of cubes **1–4** and polymers **A** and **D**.

polymers **A** and **B**, where the quantities of residual Si–H groups are greater than those of residual vinyl groups. However, the presence of two ^{29}Si resonance peaks due to residual $T^{(\text{H})}$ units (the major one at -84 ppm, and a minor one at -86 ppm) suggests the presence of the deca cube, T_{10}^{H} in T_8^{H} , a starting material for both **A** and **B**, which leads to an underestimation of the starting amount of hydrido groups.

Since all the constitutive Si units of the polymers can be directly quantified, the degree of cross-linking can also be estimated based on Si, in addition to C, according to eq 6:

$$\text{D}^{\circ}\text{cond} = \frac{\%T^{(\text{CH}_2)} + \%M^{(\text{CH}_2)}}{\%T^{(\text{CH}_2)} + \%M^{(\text{CH}_2)} + \%M^{(\text{H})} + \%M^{(\text{v})} + \%T^{(\text{H})} + \%T^{(\text{v})}} \quad (6)$$

The degree of condensation for polymers **A–D**, calculated from eq 6 (Table 1), are in excellent agreement with those found in the ^{13}C NMR study, eq 4 (see Table 1). Polymer **A** shows the lowest degree of cross-linking, **D** the highest, while **B** and **C** are in between **A** and **D**.

As stated before, some samples of each copolymer **A–D** were refluxed after they gelled up. Interestingly, all of them showed the same degrees of polymerization by NMR analysis, with or without heating. This suggests that polymerization may be thermodynamically rather than kinetically controlled, as the extent of the reaction is not affected by reaction time or temperature. Once equilibrium is reached, no further reaction occurs, and the point of equilibrium is controlled by the cube structure, as discussed above.

DRIFT Spectra of Polymers A–D. The DRIFT spectra of cubes **1–4** and polymers **A–D** are presented in Figure 5, respectively. In comparing both sets of spectra, a number of changes are immediately evident. For example, the cross-linking process transforms the vinyl νC –H bands (above 3000 cm^{-1} in the cubes) to νC –H bands at 2900 – 2890 cm^{-1} as CH_2CH_2 links form in all the polymers. The presence of Si atoms adjacent to CH_2 groups decreases the νC –H frequency by ≈ 20 cm^{-1} with respect to aliphatic νC –H bands. The remaining νC –H bands at 3065 – 3050 cm^{-1} can be assigned to the residual vinyl groups. The change in relative amounts of these residual bands reflect the degree of cross-linking seen by NMR. νSi –H bands usually appear in the 2150 – 2100 cm^{-1} range,²⁴

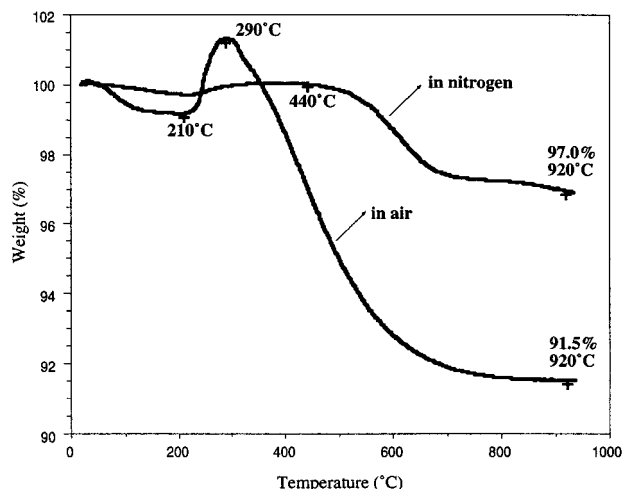


Figure 6. TGA of polymer **A** in both air and nitrogen.

but electronegative substituents on Si, e.g., O or halogens, can shift $\nu\text{Si-H}$ to $\approx 2260\text{ cm}^{-1}$, consistent with the $\approx 2270\text{ cm}^{-1}$ band observed for **1**. Cube **3**, with only one O-Si bond adjacent to the Si-H bond, exhibits a $\nu\text{Si-H}$ band $\approx 2140\text{ cm}^{-1}$. After polymerization, residual $\nu\text{Si-H}$ bands appear in positions virtually unchanged from those of the monomers, suggesting that the integrity of the cubic skeleton is retained.

Weak $\nu\text{C=C}$ bands for cubes **2** and **4** appear at 1610 and 1608 cm^{-1} , respectively. The same absorptions in the polymers are barely visible, due to their intrinsic low intensity, and low concentration as a result of the high degree of cross-linking. Bending vibrations for the CH_3 and CH_2 groups were observed at $1410\text{--}1420\text{ cm}^{-1}$. The bands at $1260\text{--}1250\text{ cm}^{-1}$ were absent from cube **1** but present in all the other cubes and polymers and are assumed to arise from $\nu\text{Si-C(H}_3\text{)}$ and/or $\nu\text{Si-C(H}_2\text{)}$ vibrations. In polymers **B-D**, the $\nu\text{Si-C}$ bands are much more intense than in polymer **A**, most likely because of the contribution of the Si- CH_3 groups of the spacer units.

The $1140\text{--}1080\text{ cm}^{-1}$ region is characteristic of strong asymmetric Si-O-Si stretches in cubic architectures, for both nonspacer and spacer compounds.²⁴ In the polymers, they appear as overlapping signals from both cube species. The slightly higher-frequency shift from **A** to **D** most likely arises from the differences in relative abundance of spacer and nonspacer species. Other bands can be assigned as Si-H rocking ($910\text{--}880\text{ cm}^{-1}$), Si-(CH_3) rocking ($850\text{--}840\text{ cm}^{-1}$), and silsesquioxane skeletal deformation vibrations ($580\text{--}560\text{ cm}^{-1}$). To sum up, DRIFT spectroscopy confirms the NMR identified structural changes that occur during hydrosilylative copolymer of cubes **1-4** and also the existence of residual functional groups.

Thermal Behavior of Polymers A-D. TGA Studies. TGA profiles of all the polymers were obtained in both N_2 and air (Figure 6, polymer **A** as an example). For polymers **A** and **B/C**, a slight mass gain is observed just above $200\text{ }^\circ\text{C}$ in air as residual Si-H groups oxidize. In polymer **D**, this oxidation is not as significant due to the lower concentration of Si-H groups. Further heating causes some mass loss above $\sim 350\text{ }^\circ\text{C}$. On heating to $950\text{ }^\circ\text{C}$, white silica residues result, with ceramic yields that correspond well to the theoretical calculations (see Supporting Information).

All the polymers showed good-to-excellent thermal stability in N_2 , apart from small mass gains that result from inevitable

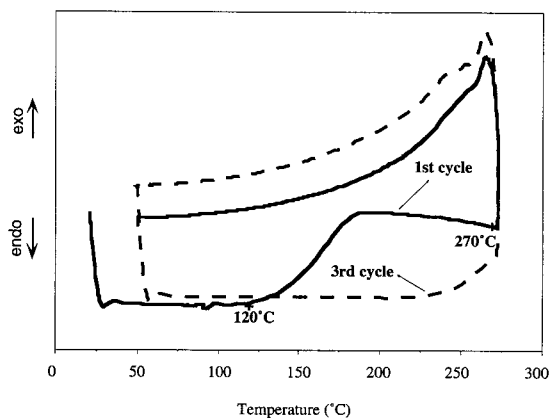


Figure 7. DSC trace of polymer **C** (in N_2).

oxidation due to traces of O_2 in the N_2 purge gas used. The first mass losses begin around $300\text{ }^\circ\text{C}$ for polymers **B-D** and $440\text{ }^\circ\text{C}$ for polymer **A**. It appears that polymer **A**, which has no siloxane spacer, is $\approx 140\text{ }^\circ\text{C}$ more stable than polymers **B-D**. This implies that the decomposition of **B-D** occurring at $\approx 300\text{ }^\circ\text{C}$ probably results from fragmentation of the siloxane spacers. Continued heating in N_2 results in gray/black oxycarbides.

DSC Studies. DSC traces (in N_2) of the first heating-cooling cycle for all four copolymers exhibit exotherms (onset temperatures $\approx 120\text{ }^\circ\text{C}$, Supporting Information) that disappear in subsequent cycles. This observation likely corresponds to thermally promoted hydrosilylation of residual Si-H and vinyl groups (Figure 7, polymer **C** used as an example). DRIFTS taken before and after DSC analysis confirms this conclusion, as intensities for the $\nu\text{Si-H}$ (2138 cm^{-1}), $\delta\text{Si-H}$ (911 cm^{-1}), $\nu\text{CH}_2=\text{CH-}$ (1416 cm^{-1}), and $\delta\text{CH}_2=\text{CH-}$ (1265 cm^{-1}) absorptions decrease significantly after cycling in the DSC. It is likely that this post-polymerization coupling of the residual groups will influence the cross-linking and, in turn, the copolymer porosity. Thus, thermal history may be an important reason why similar materials have been reported to have quite different porosities. Going from polymer **A** to **D**, the DSC exotherm onset temperature decreases from 146° to $110\text{ }^\circ\text{C}$, suggesting that the activation energy for reaction of the residual functional groups decreases from **A** to **D**. This trend agrees with the above reactivity comparison in solution.

Porosity Measurements of Polymers A-D. N_2 Sorption Analysis. Porosimetry studies provide BET surface areas and pore volume data for polymers **A-D**. Pore size analyses showed continuous distributions of pore diameters from 10 \AA to 500 \AA with the major portion occurring in the $10\text{--}100\text{ \AA}$ range (Table 1). The micropore size distribution for polymer **D** is shown in Figure 8 as an example. According to IUPAC convention, micropores are characterized by diameters less than 20 \AA , mesopores from 20 to 500 \AA , and macropores larger 500 \AA . Polymers **A-D** contain a mixture of micro- and mesopores. From Table 1, it can be seen that SSAs and pore volumes of polymer **A** are relatively higher, while those of **B** and **C** are close to those of **D**.

As shown in the pore size distribution plot, the N_2 sorption method is not capable of detecting the pores in the cubes, due to their small size ($3\text{--}4\text{ \AA}$ in theory) which does not allow Knudsen flow of N_2 . However, different techniques that "see" smaller pores can be used to solve this problem. These techniques include positron annihilation life time spectroscopy (PALS) and small angle X-ray scattering (SAXS). Molecular modeling also helps to predict what these techniques might be expected to see. Thus, a brief effort was made at modeling.

(24) Nakanishi, K. *Infrared Absorption Spectroscopy*, 2nd ed.; Holden-Day: San Francisco, CA, 1977.

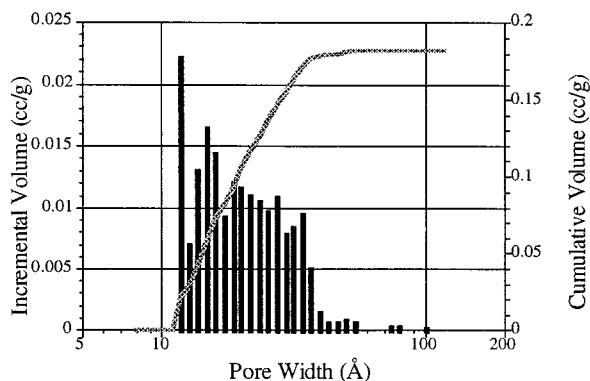


Figure 8. Pore size distribution of polymer D.

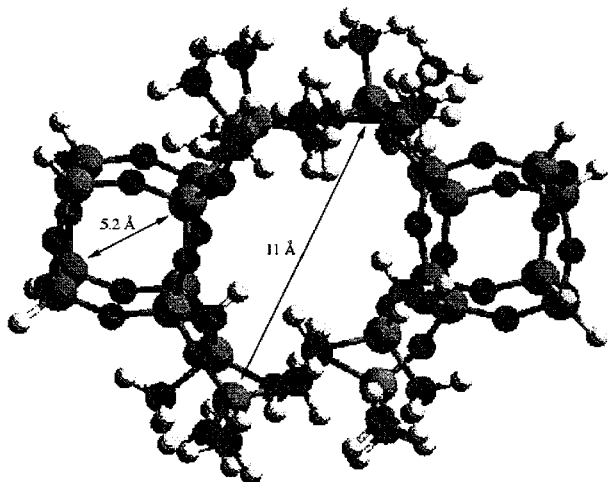


Figure 9. Molecular model of an idealized link between two silsesquioxane cubes with polymer D spaces.

Molecular Modeling. *Cerius*² molecular modeling software was used to obtain a reasonable estimate of the intercube dimensions. Initially, the structure of a single cube of **3** was created and minimized using the methods of Rappé et al.²⁵ Next, a siloxane spacer (H–O–Me₂Si–CH₂–CH₂–SiMe₂–O–H moiety of polymer D) was created, and its lowest energy conformation identified. An idealized polymer D junction was then created by connecting the corners of the parallel faces on two adjacent, minimized cubes of **3** with four siloxane spacers. The bond energies of the ensemble were reminimized to create the idealized polymer D linkage, per Figure 9.

Two distinct pore regimes can be identified in this cursory structural model: small intracube pores and large intercube pores. The intracube pores can be approximated by a 3–4 Å sphere. The intercube pores are oblong (almost cylindrical) with a 5–6 Å diameter and length of 10–12 Å. The length is in part influenced by the siloxane spacer length, while the diameter reflects the cube height.

The cube linkage presented in Figure 9 is idealized for one pair of neighboring cubes. For multiple interactions, one might expect the minimized cubes of **3** to arrange themselves in a manner reminiscent of a cubic close packed microstructure wherein each cube has ca. six nearest neighbors and can accommodate, at most, eight bonds to these six neighbors. Solid state NMR indicates that the cross-link density of polymer D is 81% of theory (eight bonds), which implies only six to seven bonds per cube, or one bond per nearest neighbor (i.e., as expected for cubic packing). This is very different from the

idealized linkage in Figure 9. Thus, the pore sizes predicted from the model will not be precise.

A three-dimensional model of the polymer D microstructure was approximated by connecting ≈ 30 minimized cubes via minimized siloxane spacers. To account for the 81% cross-link density, only seven out of eight corners on a given cube were arbitrarily connected to neighboring cubes and a minimization procedure was run. This simple model cannot provide a detailed representation of the polymer microstructure; however, it does provide a qualitative understanding of the two distinct nanopore domains also seen in the above idealized model. The dimensions of the intracube pores remain unchanged, but the intercube pores become more spherical with ≈ 10 Å diameters. The salient observation here is that the intercube pore size is still dominated by the length of the siloxane spacer. It is likely that this dimension will also be preserved in the actual microstructure.

PALS. Positron annihilation lifetime spectroscopy (PALS) is an analytical technique capable of quantifying the electron deficient regions or “nanovoids” within a dense polymeric solid. The technique is based on timing the “life” of an ortho-positronium atom (electron/positron pair abbreviated o-Ps). o-Ps atoms are known to localize in nanovoids of polymeric materials with the lifetime being related to the pore diameter within the range of 2–20 Å. Detailed descriptions of the fundamental physics behind positronium formation, annihilation, and characterization of polymers can be found in the literature.^{26a,b} For this report, it is sufficient to know that the lifetime, τ , and intensity, I , are related to the size and number of nanopores, respectively. The total nanopore content is given by

$$V_h = C v_h I_3 \quad (7)$$

$$v_h = \frac{4}{3} \pi R^3 \quad (8)$$

where R is the average nanopore radius determined from τ_3 (assuming spherical nanopores), v_h is the volume of a single nanopore, C is a normalization constant, and V_h is the nanopore volume fraction. The subscript “3” denotes lifetime and intensity values for the ortho-positronium, the parameter of interest for polymeric materials.

Analyses in terms of a single average nanovoid radius are generally sufficient to obtain a good fit of the experimental data. The cubic networks offer a challenge to PALS analysis because the modeling studies suggest a distinct bimodal distribution of nanovoids. Thus, a better fit of the experimental data might be obtained using a bimodal distribution of voids.

By default, the PFPOSFIT^{26c} analysis program deconvolutes the PALS spectra into three lifetimes and three intensities which correspond to the annihilation of the para-positronium bound state (τ_1), the free positron (τ_2), and the o-Ps bound state (τ_3). However, only the o-Ps component provides information on the size and number of nanovoids and thus is of interest to our analyses. The anticipation of a dual distribution of nanovoids suggests that we split the o-Ps component into two lifetimes (τ_3 and τ_4) and intensities (I_3 and I_4). The added parameters τ_4 and I_4 complicate the fitting procedure. To circumvent this problem, a typical three-component fit was performed, and τ_1 and τ_2 were found to have values typical of polymers. Thus τ_1

(25) Rappé, A. K.; Casewit, C. J.; Colwell, K. S.; Goddard, W. A.; Skiff, W. M. *J. Am. Chem. Soc.* **1992**, *114*, 10024.

(26) (a) Hamielec, A. E.; Eldrup, M.; Mogensen, O.; Jansen, P. *J. Macromol. Sci.-Revs. Macromol. Chem.* **1973**, *C9(2)*, 305. (b) Nakanishi, H.; Jean, Y. C. In *Positron and Positronium Chemistry*; Schrader, D. M., Jean, Y. C., Eds.; Elsevier Sci. Pub.: Amsterdam, 1988; Chapter 5. (c) Puff, W. *Comput. Phys. Commun.* **1983**, *30*, 350.

Table 2. Positron/Positronium Annihilation Lifetimes and Intensities for Polymer **D** at +30 °C and -50 °C^a

	30 °C		-50 °C	
	lifetime (ns)	intensity (rel %)	lifetime (ns)	intensity (rel %)
p-Ps	$\tau_1 = 0.200$ (fixed)	$I_1 = 34.8$ (1.4)	$\tau_1 = 0.200$ (fixed)	$I_1 = 36.4$ (0.5)
free e ⁺	$\tau_2 = 0.426$ (0.008)	$I_2 = 51.7$ (1.2)	$\tau_2 = 0.414$ (0.003)	$I_2 = 51.0$ (0.4)
o-Ps	$\tau_3 = 1.779$ (0.311)	$I_3 = 3.5$ (0.3)	$\tau_3 = 1.670$ (0.103)	$I_3 = 3.3$ (0.1)
	$\tau_4 = 6.645$ (0.385)	$I_4 = 10.0$ (0.4)	$\tau_4 = 6.063$ (0.102)	$I_4 = 9.3$ (0.1)
	30 °C		-50 °C	
	$\tau_3 = 1.779$ ns = 5.28 Å	o-Ps to τ conversions (pore diameters)	$\tau_3 = 1.670$ ns = 5.06 Å	
	$\tau_4 = 6.645$ ns = 10.90 Å		$\tau_4 = 6.063$ ns = 10.42 Å	

^a Statistical errors are given in parentheses.

was fixed to a typical value of 0.200 ns, to reduce the number of variables. This permits the addition of a fourth lifetime variable giving a reasonable fit (low variance) for two o-Ps lifetimes of 1.779 and 6.645 ns. These values correspond to pore diameters of 5 and 11 Å, respectively (Table 2) for polymer **D** at 30 °C.

The relative intensity values for I_3 and I_4 (Table 2) are consistent with the structure suggested in the molecular modeling section. Simple space filling considerations suggest that the cubes will cubic close pack with covalent siloxane linkages connecting the cube corners to form the larger intercube pores. This arrangement would produce a 1:3 statistical ratio of intra- to intercube pores. Each cube has six faces that can border on six nearest neighbors creating six intercube pores shared between nearest neighbors. The relative intensity of annihilation events is proportional to the number of nanovoids (pores). A 1:3 ratio is observed in the $I_3:I_4$ relative intensities at 30 °C (1:2.9) and at -50 °C (1:2.8). Despite the simplicity of molecular modeling study, it appears to capture the basic network microstructure. *Note that the absence of a single cube in the microstructure (a defect site) will generate pores in the 20–30 Å range (likely depending on how the linkages fill this space), accounting for the remaining porosity.*

PALS can provide only relative hole volume percent unless the normalization constant C in eq 7 is determined. A normalization technique that compares the volumetric thermal expansion coefficient to the PALS hole volume expansion coefficient²⁷ was employed in this work. A Perkin Elmer TMA7 was used to measure the linear expansion coefficient for **D** polymer and, assuming isotropic expansion, a volumetric expansion coefficient of 4.8×10^{-4} °C⁻¹ was measured. The microscopic PALS expansion coefficient was determined. Using eq 7 for the hole volume V_h , the nanovoid expansion coefficient can be obtained through the relationship

$$\alpha_{\text{pals}} = \left(\frac{\Delta V_h}{\Delta T} \right) \left(\frac{1}{V_{h,\text{ref}}} \right) = \left(\frac{(Cv_h I_1)_{T_1} - (Cv_h I_3)_{T_2}}{T_1 - T_2} \right) \left(\frac{1}{(Cv_h I_1)_{T_1}} \right) \quad (9)$$

where $V_{h,\text{ref}}$ was taken to be at 30 °C. This procedure, and the combined volumes of the inter- and intracube components for polymer **D** (-50 to 30 °C), gives a PALS volumetric expansion coefficient of 3.5×10^{-3} °C⁻¹ which is an order of magnitude greater than the macroscopic expansion coefficient. This is typical because PALS measures the expansion of nanovoids, which expand at a much faster rate than the bulk.²⁸ Such behavior, where the microscopic expansion coefficient is an

(27) Hristov, H. A.; Bolan, B.; Yee, A. F.; Xie, L.; Gidley, D. W. *Macromolecules* **1996**, *29*, 8507.

(28) Yang, L.; Hristov, H. A.; Yee, A. F.; Gidley, D. W.; Bauchiare, D.; Halary, J. L.; Monnerie, L. *Polymer* **1995**, *36*, 3997.

(29) Slutsker, A. I.; Filippov, V. E. *Polym. Sci. U.S.S.R.* **1988**, *30*, 2556.

Table 3. Typical and Experimental Volumetric Expansion Coefficients

expansion coeff method	expansion coeff (°C ⁻¹)
dilatometry in thermoplastics	2.5×10^{-4}
dilatometry in thermoset (epoxy)	1.8×10^{-4}
dilatometry in polymer D	4.8×10^{-4}
PALS nanovoid expansion in thermoplastics	3.0×10^{-3}
PALS nanovoid expansion in thermoset (epoxy)	2.5×10^{-3}
Polymer D via changes in PALS total hole volume	3.5×10^{-3}
Polymer D via changes in PALS intercube radius	1.1×10^{-3}

order of magnitude larger than the macroscopic, is also consistent with wide angle X-ray scattering measurements performed on amorphous polymers.²⁹ Both the TMA and PALS expansion coefficients are typical for both thermoset and thermoplastic polymers (Table 3).²⁸

Polymer **D** can be thought of as a nanocomposite consisting of a polymer matrix (flexible siloxane spacers) filled with nano-sized particles (cubes). Polymer glasses generally exhibit thermal expansion coefficients (CTEs) more than an order of magnitude larger than typical inorganic glasses. *Table 3 indicates that the polymer D CTEs are consistent with those of a polymeric material suggesting that expansion is dominated by the intercube domains.* Thus, most of the expansion should originate from the large intercube voids. Table 2 bears this out as the τ_3 values for the small intracube pores at -50 and 30 °C (1.7 and 1.8 ns, respectively) are within experimental error. Thus, the majority of the expansion must derive from the inter-cube domains. A CTE based on the expansion of only the intercube pores (1.1×10^{-3} °C⁻¹) is the same order of magnitude as the total PALS CTE supporting this conclusion. *The combination of cubes with flexible spacers provides a route to materials with porosity reminiscent of a zeolite but the properties of a polymer.*

The CTEs determined above can be used to calculate the absolute volume fraction of PALS pores. Following published procedures, polymer **D** possesses 14 % microporosity at 30 °C.²⁷ Furthermore, the I_3 and I_4 intensities can be used to separate the 14% microporosity into the volume fractions for intra- and intercube domains. Thus, the absolute volume fractions of intra- and intercube micropores are 4 and 10%, respectively. Note that these volume fractions are extremely high. Typical thermoplastic and thermoset polymers have 5–6 vol % micropores at the glass transition temperature.³⁰ At 30 °C, polymer **D** is well below its T_g , yet it exhibits over twice the microporosity of a typical organic polymer. Note that this volume fraction represents only those pores “seen” by PALS (2–20 Å) but not the large scale mesoporosity “seen” by the BET and SAXS technique.

(30) Hristov, H. A.; Soles, C. L.; Bolan, B. A.; Gidley, D. W.; Yee, A. F. *Polym. Mat. Sci. Eng.* **1997**, *76*, 431.

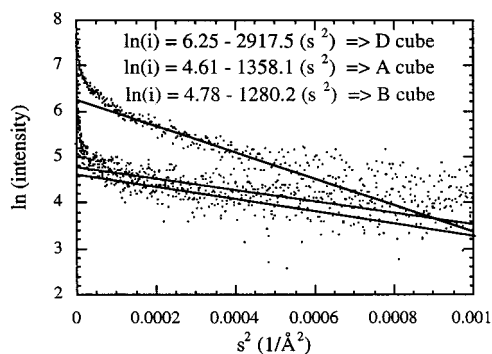


Figure 10. Guinier plot from the SAXS data for the polymers **A**, **B**, and **D**.

It is useful to compare PALS microvoid volumes to BET microvoid volumes for polymer **D** (Figure 8). The BET void distribution for polymer **D** shows a significant volume fraction of pores at 10–11 Å that appears to overlap the intercube pores seen by PALS. If the two techniques actually sample the same pore volume, normalization of the PALS data becomes trivial. For the 10–11 Å component, the BET results indicate an incremental pore volume of 0.022 cc/g with a total volume of 0.18 cc/g which converts to a pore volume fraction of $0.022/0.18 = 12\%$. Using the BET data as a normalization factor, one obtains an absolute intercube pore volume of 12%, an intracube pore volume of 4%, and a total PALS pore volume of 16%. This then is the volume fraction of micropores.

The absolute hole volumes determined from both normalization methods (using either the CTEs or the BET data) are self-consistent. Note that the overall porosity is $\gg 15\%$ as PALS cannot see larger voids. BET “sees” the large intercube pores, however it is not sensitive to intracube pores and misses 4 vol % porosity. This demonstrates the utility of using PALS and BET simultaneously to obtain a complete picture. Small angle X-ray scattering (SAXS) provides a check on the other two methods.

X-ray Scattering. SAXS provides an alternate method of measuring porosity. X-ray scattering can be used to quantify structural features where distinct differences in electron density exist, e.g., for either second phase particle or voids. A Guinier approximation of particle scattering can be used to derive information on the size of nanovoids.³¹ The Guinier approximation is valid for calculating the size of monodisperse voids when a plot of $\ln I(s)$ versus s^2 , [$I(s)$ = scattering intensity and s = diffraction vector, $s = 2 \sin \theta/\lambda$], give a straight line in the low s^2 region. However, the Figure 10 Guinier plots of SAXS data for polymer **D** exhibit curvature indicating a distribution of void sizes. Thus, the Guinier approximation can only be used to compare relative trends between materials.

Guinier plots for polymers **A**, **B** and **D** (30 °C) are shown in Figure 10. Although Figure 10 extends only to 0.001 in s^2 , at larger s^2 values (from 0.004 to 0.005 Å⁻²) all three materials exhibit equal slopes indicative of voids 5–7 Å in diameter; consistent with the molecular modeling and PALS results for intracube pores. While a rigorous correlation between the size and slope is not possible, all three materials behave similarly in this range as expected, given that they all have identical intracube pores.

Note that in Figure 10 polymer **D** behaves markedly different from either **A** or **B**. In the 0.0002–0.0004 s^2 regime, the slope for **D** increases by a factor of 2 over the slopes for **A** and **B**.

This suggests that strong scattering from pores in this size regime for **D** is not seen for either **A** or **B**. Based on the BET pore distributions for these materials, polymer **D** has a much narrower pore size distribution than seen for either polymers **A** or **B**. Furthermore, this sharp distribution is clustered about a mean size of 20–30 Å. The narrow distribution suggests there should also be high concentration of scattering entities (pores) in this size range. The Guinier plot slope in the regime where **D** differs from the **A** and **B** materials, nominally corresponds to a diameter of 38 Å. This is larger than expected from the BET distribution (20–30 Å). However, one must remember that the slope of the Guinier plot in this region is actually enhanced, or convoluted, by scattering contributions of smaller entities at larger s^2 values, as discussed above. A slope larger than the mean size predicts is consistent with this fact. Moreover, the intensity of X-rays scattered from spherical particles scales approximately with one over the particle radius to the fourth power.³² Thus, larger pores in **A** and **B** polymers will cause intensities to drop off more rapidly at smaller angles. Such behavior is also observed in Figure 9.

Wide angle X-ray scattering was performed on **D** in the 2 θ region from 2–20° (see Supporting Information). A typical amorphous polymer halo is observed centered at 17.4° 2 θ . A second low angle amorphous peak is observed at 7.0° 2 θ . Low angle amorphous peaks of this nature are common in cross-linked epoxy networks,³³ although the low angle peak here is far more intense than those reported in epoxies. The exact meaning of this low angle peak is not straightforward. Bragg and modified Bragg peak analyses suggest average interatomic distances of 13–16 Å.³⁴ While such an interpretation of a broad, low-angle peak is questionable, this spacing approximates the length of one cube plus one siloxane linkage, which should form a basic repeat unit for the network. *Additional work is required to establish the network topology more accurately, but the data are entirely consistent with simple cubic packing as discussed above.*

It was demonstrated above that the SAXS data is, generally speaking, in good qualitative agreement with the molecular modeling, PALS, and the BET data. Detached, each of these techniques provides insufficient information to provide a detailed description of the polymer microstructure. Taken *in toto*, all of the techniques provide a much clearer view of the microstructure, although further refinement is possible.

Conclusions

To sum up, the following have been established in this work:

(1) Cubes **3** and **4** are more reactive than **1** and **2**, most likely because of the improvements that the Me₂SiO spacer groups provide in segmental mobility and in reactive group flexibility and accessibility.

(2) Solid state ¹³C and ²⁹Si MAS–NMR analyses indicate that β -hydrosilylation is the primary process that occurs during copolymerization, for all polymers studied. The degree of cross-linking, measured on the basis of the amounts of reacted and unreacted groups, increases on going from polymer **A** to **B(C)**, to **D**. Similar trends were found by DRIFTS.

(3) Thermal analyses indicate that polymers **A–D** are thermally stable to temperatures >300 °C. Post-synthesis heat treatments at >100 °C promote further reaction of residual functional groups, which may change polymer porosities.

(32) Rayleigh, L. *Proc. Roy. Soc. (London)* 1911, A-84, 25.

(33) (a) Lovell, R.; Windle, A. H. *Polymer* 1991, 30, 593. (b) Kumar, S.; Adams, W. W. *Polymer* 1987, 28, 1497.

(34) Klug, H. P.; Alexander, L. E. *X-Ray Diffraction Procedures for Polycrystalline and Amorphous Materials*; Wiley: New York, 1974; p 847.

(31) Guinier, A.; Fournet, G. *Small Angle Scattering of X-Rays*; John Wiley & Sons: New York, 1955.

(4) Nitrogen sorption analyses show that **A** has the highest SSA and pore volume and **D** the lowest among the four polymers. The pore size distributions in all the polymers were studied using three complementary techniques. Nitrogen sorption provided a view of the pore sizes in the 10–500 Å, while PALS allowed identification of pores in the cubes (~ 3 Å), and in between of the cubes (10–11 Å), and SAXS provided overlapping confirmation of the first two methods.

Acknowledgment. We acknowledge FAA for their generous support of this work through Grant No. 95-G-026. This work was also supported in part through the University of Michigan Dental Materials Research Center under NIDR Grant No. DE09296-06. We thank Rita Baranwal for help with the nitrogen

sorption analyses and Jocelyne Maquet for assistance with the solid state NMR experiments. C.L.S., A.F.Y., and H.A.H. thank the Air Force Office of Scientific Research for support under Grant No. F49620-95-1-0037. R.M.L. and F.B. thank NSF for an International Programs NSF/CNRS travel grant.

Supporting Information Available: Tables of ^{13}C peak assignments, ^{13}C CP NMR data, ^{29}Si peak assignments, ^{29}Si CP NMR data, and summary of TGA and DSC data for polymers **A–D** and figures of magnetization evolutions vs t_1 for the ^{29}Si sites of polymers **A** and **D** and wide angle X-ray scattering of polymer **D** (8 pages, print/PDF). See any current masthead page for ordering and Web access instructions.

JA9808853